Theoretical Rate Constants for the $NH_3 + NO_x \rightarrow NH_2 + HNO_x$ ($x = 1, 2$) Reactions by ab Initio MO/VTST Calculations

A. M. Mebel, E. W. G. Diau, M. C. Lin,* and K. Morokuma*

Cherry L. Emerson Center for Scientific Computation and Department of Chemistry, Emory University, Atlanta, Georgia 30322

Received: December 8, 1995; In Final Form: February 9, 1996[⊗]

Potential energy surfaces for the reactions of NH_3 with NO_x ($x = 1, 2$) have been studied by ab initio molecular orbital Gaussian 1 (G1) and Gaussian 2 (G2) methods. Both reactions have been shown to be endothermic and to proceed by the abstraction of a hydrogen atom from ammonia to produce NH_2 and HNO_x. The calculated heats of reaction are in close agreement with experimental measurements. Reaction 1, $NH_3 + NO$, does not have a reverse barrier at the G2 level of theory. Reaction 2, $NH_3 + NO_2$, can occur by three channels, leading to HNO_2 (2a), *cis*-HONO (2b), and *trans*-HONO (2c), and each mechanism involves the formation of $NH_2 \cdot HNO_2$ or $NH_2 \cdot HONO$ intermediate complexes. Mechanism 2b has been found to be dominant. Theoretical rate constants for (1), (2b), and their reverse reactions have been computed by VTST in conjunction with detailed balancing for the temperature range of 300−5000 K. The following least-squares fitted expressions are recommended for practical applications: $k_1 = 1.72 \times 10^{-17} T^{1.73} e^{-28454/T}$, $k_{-1} = 6.02 \times 10^{-17} T^{1.63} e^{630/T}$, $k_{2b} = 3.92 \times 10^{-23} T^{3.41} e^{-11301/T}$, $k_{-2b} = 11.8 \times 10^{-23} T^{3.02} e^{2487/T}$, in $cm^3/(molecule \cdot s)$. The apparent activation energies calculated variationally for $300 \leq T \leq 1000$ K, 58.3 and 25.6 kcal/mol for (1) and (2), respectively, agree well with experiments.

Introduction

The reactions of NH_3 with NO_x, particularly their reverse processes,

$$NH_2 + HNO \rightarrow NH_3 + NO$$

$$NH_2 + HONO \rightarrow NH_3 + NO_2$$

are relevant to the NH_3−de-NO_x chemistry[1−3] and to the combustion of ammonium dinitramide (ADN).[4,5] NH_2 is the key reductive agent in these systems, and like its isoelectronic OH species, it is fairly reactive. To our knowledge, no direct experimental measurements of the rate constants for the above reactions have been carried out, probably because it is difficult to prepare laboratory conditions for reliable kinetic determination.

As part of our effort to establish a predictive mechanism for the H/N/O system in general[6−12] and the NH_3−NO_x reactions in particular,[13,14] we have performed high-level ab initio molecular orbital calculations for the aforementioned reactions so as to provide a reliable estimate of their effects on the de-NO_x process and ADN combustion reactions at high temperatures. The computed energies and molecular parameters for the reactants, transition states, and products were used to calculate the bimolecular rate constants of the forward and reverse directions for both processes over the broad temperature range of 300−5000 K, employing the variational transition-state theory method (VTST).[15]

Theoretical Methods and Computational Procedure

The geometries of various structures of the reactants, products, intermediates, and transition states for the reactions $NH_3 + NO$ (1) and $NH_3 + NO_2$ (2) have been optimized at the UMP2 level with the 6-311G(d,p) basis set.[16] Vibrational frequencies have been calculated at the same level of theory for characterization of the nature of stationary points and zero-point energy corrections (ZPEs) and to compute the entropies and Gibbs free energies. All the intermediates have been positively identified for a minimum number of imaginary frequencies (NIMAG = 0) or transition states (NIMAG = 1). For anharmonicity correction, the calculated UMP2/6-311G(d,p) frequencies and ZPE were scaled by 0.95.[16]

In order to obtain more reliable energies of various structures, we used the G1 and G2 methods.[17] The conventional G1 scheme consists of a series of calculations to approximate a QCISD(T)/6-311+G(2df,p)//MP2/6-311G(d,p) calculation with an additional "higher order correction" based on the number of paired and unpaired electrons. The G2 method uses an additional correction to obtain an estimate of the QCISD(T)/6-311+G(3df,2p) energy. In our procedure, we used the MP2/6-311G(d,p)-optimized geometries and scaled ZPE, and for the radicals, we used projected UMP4 and UMP2 (PUMP4 and PUMP2) energies which give more reliable results for open-shell systems than the regular (unprojected) MP4 and MP2 methods. These calculational schemes were referred to as G1-(PU) and G2(PU).[18] The G2 method is somewhat more accurate than G1; however, it requires substantially larger computational efforts. Hence, we used the G2(PU) approach for the $NH_3 + NO$ reaction and G1(PU) for $NH_3 + NO_2$. All the calculations have been performed using the Gaussian 92/DFT program.[19]

Variational transition-state theory (VTST) has been employed to compute the reaction rate constants. VTST allows us to account for the temperature effects on the reaction rates better than the conventional transition-state theory (CTST) because it considers the variation of transition states at the Gibbs free-energy hypersurface with temperature. With the VTST approach, the rate constant at temperature T is expressed as[15]

$$k = (k_B T/h) \exp[-\Delta G^*_v(T)/RT] \quad (1)$$

where $\Delta G^*_v(T)$ is the Gibbs free-energy change from the reactants to the transition state at T. In order to locate the maximum ΔG^* for each temperature, we performed intrinsic

[⊗] Abstract published in *Advance ACS Abstracts,* April 1, 1996.

S0022-3654(95)03644-6 CCC: $12.00

TABLE 1: Total (hartree) and Relative (kcal/mol) Energies of $NH_3 + NO$, $NH_2 + HNO$, TS1, and the Structures along IRC, Calculated at the UMP2/6-311G(d,p) and G2(PU) Levels of Theory

		energies		
species	ZPE[a]	UMP2/ 6-311G(d,p)	UMP2/ 6-311G(d,p) +ZPE	G2(PU)
$NH_3 + NO$[b]	23.6[d]	−186.028 28	−185.990 73	−186.209 27
R5 ($s = -0.5$)[c]	23.8[e]	39.4	39.7	37.6
R4 ($s = -0.4$)[c]	23.8[e]	45.7	45.9	42.6
R3 ($s = -0.3$)[c]	23.3[e]	57.0	56.7	49.4
R2 ($s = -0.2$)[c]	22.9	61.6	61.0	52.7
R1 ($s = -0.1$)[c]	20.6	62.0	59.0	53.1
TS1 ($s = 0$)[c]	20.2	64.7	61.3	55.2
F1 ($s = +0.1$)[c]	20.6	64.5	61.5	56.0
F2 ($s = +0.2$)[c]	20.9	64.3	61.7	57.0
F3 ($s = +0.3$)[c]	21.1	64.0	61.6	57.3
F4 ($s = +0.4$)[c]	21.1	63.7	61.3	57.5
F5 ($s = +0.5$)[c]	21.2	63.3	61.0	57.5
$NH_2 + HNO$	19.9	64.1	60.4	57.5

[a] Zero-point vibrational energies are calculated at the UMP2/6-311G(d,p) level and scaled by 0.95. [b] Total energies. Relative energies in the rest of the table are given with respect to $NH_3 + NO$. [c] s is the reaction coordinate in amu$^{1/2}$·bohr. [d] Vibrational frequency for NO was calculated at the QCISD/6-311G(d,p) level. [e] Some vibrational frequencies were corrected, as described in the text.

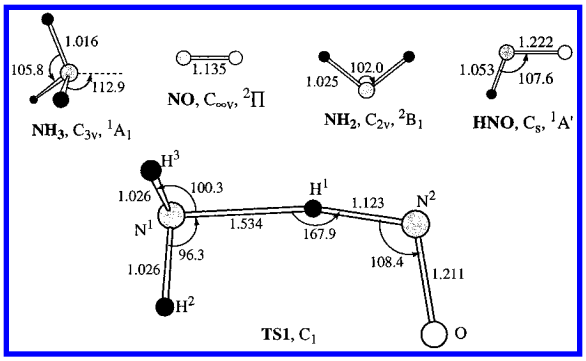

Figure 1. UMP2/6-311G(d,p)-optimized geometries (in Å and deg) of NH_3, NO, NH_2, HNO, and abstraction transition state TS1.

reaction coordinate (IRC) calculations in the vicinity of the transition states for the rate-controlling steps using the algorithm[20] implemented in Gaussian 92.

The $NH_3 + NO \rightarrow NH_2 + HNO$ Reaction

Potential Energy Surface. The reaction of ammonia with NO can proceed by direct abstraction of a hydrogen atom of NH_3 by NO to produce the NH_2 radical and HNO. As seen in Table 1, the reaction is calculated to have a high endothermicity, 57.5 kcal/mol, at the G2(PU) level, which is close to the experimental value of 58.5 kcal/mol. At the UMP2/6-311G(d,p) + ZPE level, the energy of reaction, 60.4 kcal/mol, is not far from the experimental value, either. Neither the reactant complex, $H_2NH\cdots NO$, nor the product complex, $H_2N\cdots HNO$, was found. The structure of the transition state TS1, optimized using the UMP2/6-311G(d,p) method, is shown in Figure 1. TS1 is a late transition state; its geometry is closer to that of $NH_2 + HNO$ than to that of $NH_3 + NO$, as could be expected from the endothermic character of the reaction. The H^1N^2 distance in TS1 is longer only by 0.07 Å than that in HNO, while the N^1H^1 distance is elongated by 0.5 Å as compared to the NH bond length in NH_3. The $N^1H^1N^2$ fragment is nearly collinear, with the $N^1H^1N^2$ angle of 167.9°, and the $H^2N^1H^1N^2O$ group is almost coplanar. The geometry of TS1 is similar to the structure of the hydrogen-abstraction transition state for the isoelectronic $H_2O + NO \rightarrow OH + HNO$ reaction, calculated by Soto et al.[21] The latter TS has a somewhat later character than the former, with the forming HN bond length of 1.054 Å, because of the higher endothermicity of the $H_2O + NO \rightarrow OH + HNO$ reaction, 69.4 kcal/mol.

The abstraction barrier at TS1 is 61.3 kcal/mol above the reactants at the UMP2/6-311G(d,p) + ZPE level, and the barrier for the reverse $NH_2 + HNO \rightarrow NH_3 + NO$ reaction is only 0.9 kcal/mol with this approximation. The G2(PU) method reduces the relative energy of TS1 to 55.2 kcal/mol, i.e., below the $NH_2 + HNO$ products. Therefore, one can conclude that for the reverse reaction, the barrier is small or nonexistent.

IRC Calculations. Intrinsic reaction coordinate calculations in the vicinity of TS1 provide geometries, energies, and $3N - 7$ projected vibrational frequencies necessary to compute the Gibbs free-energy changes which are used in the VTST calculation of the rate constant. We calculated 10 structures along IRC for the reaction coordinate values s from −0.5 to 0.5 amu$^{1/2}$·bohr. The points are denoted as R5−R1 and F1−F5 for the reverse and forward side of IRC, respectively. The changes of some geometric parameters, relative UMP2/6-311G(d,p) energies and vibrational frequencies along IRC, are shown in Figure 2a−d. Only the N^1H^1 and H^1N^2 distances change significantly during the reaction, because the former bond is breaking and the latter is forming. The $N^1H^1N^2$ angle is slightly decreasing after the barrier is cleared. More complicated behavior is found for the vibrational frequencies, as seen in Figure 2c and in Table 2. While at $N^1H^1 \geq 1.435$ Å, they change smoothly and converge to the frequencies of $NH_2 + HNO$, at $N^1H^1 \leq 1.390$ Å, one can see oscillations of some frequencies. For example, at $N^1H^1 = 1.39$ Å (R3, reaction coordinate s is −0.3 amu$^{1/2}$·bohr), the Q_1 is calculated to be imaginary, 930i cm^{-1}; Q_3, 337 cm^{-1}, and Q_6, 945 cm^{-1}, are too low. At $N^1H^1 = 1.285$ Å ($s = -0.5$ amu$^{1/2}$·bohr), the Q_{11} mode has an extremely high frequency, 4932 cm^{-1}! These results are artifacts of using the unrestricted MP2 method for frequency calculations and are attributed to spin contamination. As discussed in the literature,[9,22] the errors in UMP2-calculated frequencies are correlated with $d\langle S^2\rangle/dR$, where $\langle S^2\rangle$ is the expectation value of the spin operator at the UHF level before projection and R is a geometric parameter. The higher the derivative of the spin contamination, the higher the error in vibrational frequency. For instance, for NO, where $d\langle S^2\rangle/dR$ is 1.25, the error encountered is about 1400 cm^{-1}.[22] The use of the erroneous frequencies at $s = -0.5$, −0.4, and −0.3 can seriously affect the ΔG^* values of R5, R4, and R3. Therefore, we corrected some frequencies for these structures using linear interpolation along the N^1H^1 coordinate. The adjusted frequencies are presented in Table 2; the corrected picture of frequency change is shown in Figure 2d. We have also corrected the UMP2 frequency of NO using a QCISD value.[9] An interesting feature is the decrease of the Q_9 frequency from the reactants to TS1, and its increase after the barrier is cleared. In the early phase of the reaction, this mode corresponds to the N^1H^1 stretch, and in the late phase, it is the H^1N^2 stretch vibrations. In the vicinity of TS1, these two modes are mixed, and the frequency is low. Q_9 and Q_6 frequencies reach their minima at TS1. As a result, ZPE also has the lowest value at TS1, and it increases when the reaction coordinate is negative or positive. As seen in Figure 2b, summation of the UMP2 energy with ZPE gives the energy profile with the minimum approximately at R1 ($s = -0.1$) and the maximum shifted away from TS1, to F2 ($s = 0.2$).

VTST Calculations of the Rate Constant. Since TS1 and the structures along IRC were optimized at the UMP2/6-311G-

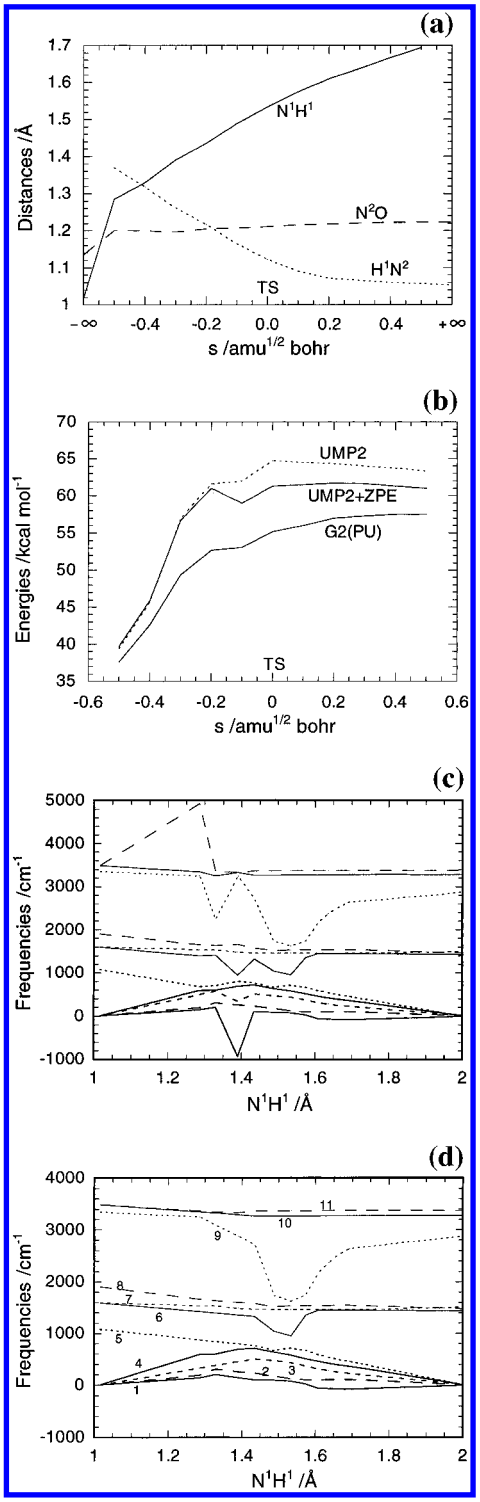

Figure 2. (a) Changes of some geometric parameters for the NH_3 + NO system along IRC as functions of the reaction coordinate *s*. (b) Changes of the relative UMP2/6-311G(d,p), UMP2/6-311G(d,p) + ZPE, and G2(PU) energies along IRC as functions of *s*. (c) Changes of vibrational frequencies for the NH_3 + NO system as functions of *s*. (d) Corrected vibrational frequencies for the NH_3 + NO system.

(d,p) level, we looked for maxima of ΔG^* at different temperatures at this level of theory. ΔG^* was computed using the corrected vibrational frequencies from Table 2 and moments of inertia shown in Table 3. One can see that the structures F2−F5 have one imaginary frequency, and the lowest frequency of F1 has a very small value, 25 cm^{-1}. The normal mode, corresponding to these frequencies, is rotation of the NH_2 and HNO fragments around the N···H axis. Therefore, in the partition function calculations, we replaced the vibration by free

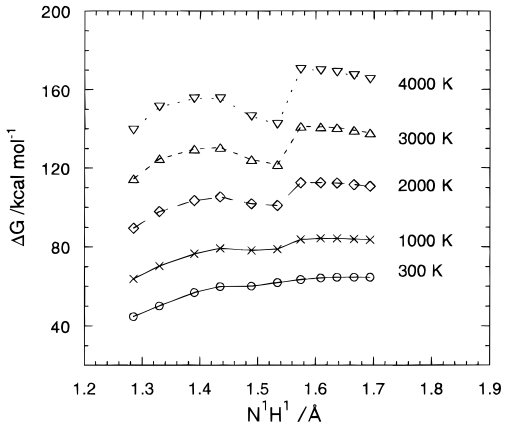

Figure 3. Change of ΔG along IRC for the NH_3 + NO system as a function of *s* at different temperatures. $\Delta H°(0)$'s were calculated at the UMP2/6-311G(d,p) + ZPE level.

rotation. Moments of inertia for the rotation about the N···H bond, calculated from the geometries, are also presented in Table 3. For TS1, with the lowest frequency of 74 cm^{-1}, the substitution of vibration by rotation has no noticeable effect on the value of ΔG^*.

The change of ΔG^* along IRC in the temperature range of 300−5000 K is shown in Figure 3. The maximum of the relative free energy was determined for each temperature in the interval by using polynomial fitting of computed ΔG^* values. Its location changes from $s = 0.42$ amu$^{1/2}$·bohr at 300 K to $s = 0.15$ amu$^{1/2}$·bohr at 5000 K. As seen in Figure 3, the ΔG^* curves exhibit an oscillatory change along the reaction coordinate at higher temperatures in the vicinity of TS1. This is attributed to the entropy factor in the Gibbs free energy which is larger for small absolute values of *s* due to the aforementioned behavior of the frequencies. Potential energies of the maxima for each temperature were interpolated on the basis of the G2-(PU) energies for the structures F1−F5 and used to correct $\Delta G_v^*(T)$ from UMP2 to the G2(PU) level. The corrected relative free energies were employed to compute the reaction rate constant for each temperature using eq 1. Tunneling correction was not used in the calculations because the reverse reaction has no barrier at the G2(PU) level. The three-parameter expressions for the rate constant k_1 and its reverse rate constant k_{-1}, evaluated with the calculated equilibrium constant K_1 by the relationship $k_{-1} = k_1/K_1$, for the temperature range of 300−5000 K, are given in cm^3/(molecule·s) by

$$k_1 = 1.72 \times 10^{-17} T^{1.73} e^{-28454/T}$$

$$k_{-1} = 6.02 \times 10^{-18} T^{1.63} e^{630/T}$$

The Arrhenius plot for k_1 and k_{-1} is shown in Figure 4. The value of k_1 reported by Hanson from his shock tube measurement,[23] $8.3 \times 10^{-10} e^{-25161/T}$, is significantly higher than our calculated value. However, Hanson's rate constant does not seem to be reliable because he used an estimate for activation energy of 50.0 kcal/mol, much lower than the experimental reaction endothermicity. In our k_1, the apparent activation energy, 58.3 kcal/mol, calculated variationally for the temperature range $300 \le T \le 1000$ K, is close to the experimental enthalpy change, 58.5 kcal/mol.[24] The calculated equilibrium constant, $K_1 = 6.34 \exp(-29\,084/T)$, is close to that computed on the basis of JANAF tables,[24] $K_1 = 9.21 \exp(-29603/T)$.

The rate constant for the reverse NH_2 + HNO reaction is similar but somewhat smaller than the rate coefficient calculated by Soto et al.[21] for the isoelectronic OH + HNO reaction, *k*(OH

TABLE 2: Vibrational Frequencies (cm^{-1}) for $NH_3 + NO$, $NH_2 + HNO$, TS1, and the Structures along IRC, Calculated at the UMP2/6-311G(d,p) Level and Scaled by 0.95

species	ω_1	ω_2	ω_3	ω_4	ω_5	ω_6	ω_7	ω_8	ω_9	ω_{10}	ω_{11}
$NH_3 + NO$	0	0	0	0	1073	1593	3382/1861[a]	3349	3485 s	3485 m	
R5 ($s = -0.5$)[c]	138	187	484/324[b]	585	679/873[b]	1394/1424[b]	1532	1660	3251	3342/3346[b]	4932/3362[b]
R4 ($s = -0.4$)[c]	199	298	572/378	596	695/839[b]	1411/1395[b]	1530	1633	2240/3092[b]	3250/3323[b]	3342
R3 ($s = -0.3$)[c]	930*i*/143[b]	252	337/450[b]	689	801/795[b]	945/1357[b]	1490	1666/1604[b]	3242/2881[b]	3327/3292[b]	3335
R2 ($s = -0.1$)[c]	101	230	504	712	761	1329	1469	1583	2722	3269	3362
R1 ($s = -0.1$)[c]	90	176	466	631	663	1043	1462	1516	1731	3270	3367
TS1 ($s = 0$)[d]	74	119	432	576	710	955	1462	1532	1625	3271	3369
F1 ($s = 0.1$)[c]	25	97	368	505	666	1347	1462	1539	1737	3272	3369
F2 ($s = 0.2$)[c]	61*i*	97	300	453	584	1453	1464	1539	2172	3273	3372
F3 ($s = 0.3$)[c]	67*i*	103	275	420	531	1454	1464	1542	2375	3274	3372
F4 ($s = 0.4$)[c]	76*i*	102	244	388	489	1451	1463	1544	2534	3277	3374
F5 ($s = 0.5$)[c]	79*i*	103	221	359	455	1449	1463	1546	2647	3278	3375
$NH_2 + HNO$	0	0	0	0	0	1431	1511	1469	2883	3276	3369

[a] QCISD/6-311G(d,p) frequency for NO. [b] The second number is the frequency value, corrected using linear interpolation, as alluded to in the text. [c] For the structures along IRC, $3N - 7$ frequencies projected out of the reaction coordinate were calculated. [d] The imaginary frequency value is $1571i$ cm^{-1}.

TABLE 3: Moments of Inertia for the Structures along IRC (10^{-40} g × cm^2)

species	I_x	I_y	I_z	$I_{NH_2/HNO}$[a]
R5	18.0	147.8	163.2	
R4	18.1	146.7	162.2	
R3	18.0	146.8	162.2	
R2	18.2	146.9	162.5	
R1	18.3	147.0	162.7	
TS1	18.4	147.2	163.0	3.23
F1	18.6	147.7	163.7	3.22
F2	18.8	148.5	164.7	3.21
F3	19.1	149.5	166.0	3.20
F4	19.3	150.6	167.2	3.18
F5	19.5	151.6	168.5	3.17

[a] The moment of inertia for the molecule rotation around the N···H axis.

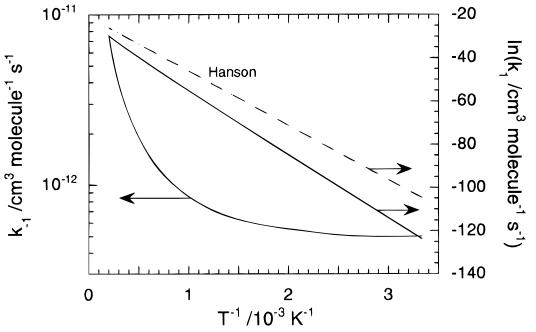

Figure 4. Arrhenius plot of the forward and reverse rate constants for the $NH_3 + NO \rightarrow NH_2 + HNO$ reaction.

$+ HNO) = 2.15 \times 10^{-17}T^{1.884}e^{481/T}$, reflecting the fact that the OH radical is more reactive than NH_2 and that the exothermicity of the $NH_2 + HNO$ reaction is about 11 kcal/mol lower than that of the $OH + HNO$ reaction; neither has a noticeable barrier.

The $NH_3 + NO_2$ Reaction

Structure and Energetics of Intermediates and Transition States. The NO_2 radical can abstract a hydrogen atom from NH_3 by the nitrogen or the oxygen end. In the first case, the HNO_2 molecule is formed; otherwise, an HONO structure is produced. The species with the $H_1N_1O_2$ stoichiometry has three most stable isomers: the nitro isomer HNO_2 and *cis*- and *trans*-nitrito structures HONO. These defines three different channels of the $NH_3 + NO_2$ reaction:

$$NH_3 + NO_2 \rightarrow NH_2 + HNO_2 \qquad (2a)$$

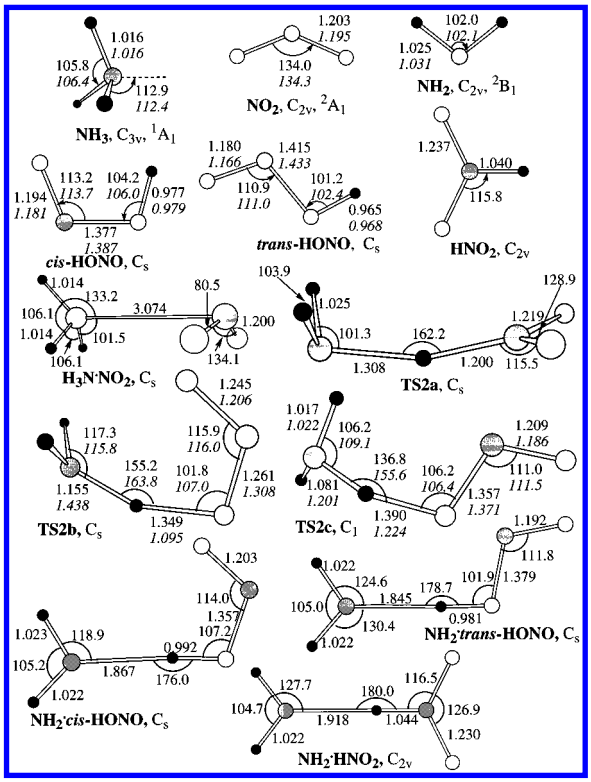

Figure 5. UMP2/6-311G(d,p)-optimized geometries (in Å and deg) of the reactants, products, intermediates, and transition states for the $NH_3 + NO_2$ reaction. Italic numbers for the reactants, products, TS2b, and TS2c show B3LYP/6-311G(d,p)-optimized parameters.

$$NH_3 + NO_2 \rightarrow NH_2 + cis\text{-HONO} \qquad (2b)$$

$$NH_3 + NO_2 \rightarrow NH_2 + trans\text{-HONO} \qquad (2c)$$

Our UMP2/6-311G(d,p)-optimized geometries for the reactants, products, transition states, and intermediates of these reactions are shown in Figure 5. Geometry optimization for the transition states and intermediates was performed without any symmetry constraints, but most of them were found to have C_s symmetry. The G1(PU)-calculated potential energy surfaces are presented in Figure 6.

The reactions (2a)−(2c) are endothermic, though to a smaller extent than the $NH_3 + NO \rightarrow NH_2 + HNO$ reaction. *trans*-HONO is the most stable isomer, and (2c) has the lowest endothermicity, 33.4 and 26.4 kcal/mol at the UMP2/6-311G(d,p) + ZPE and G1(PU) levels, respectively, in comparison with the experimental value of 29.5 kcal/mol. The heats of the

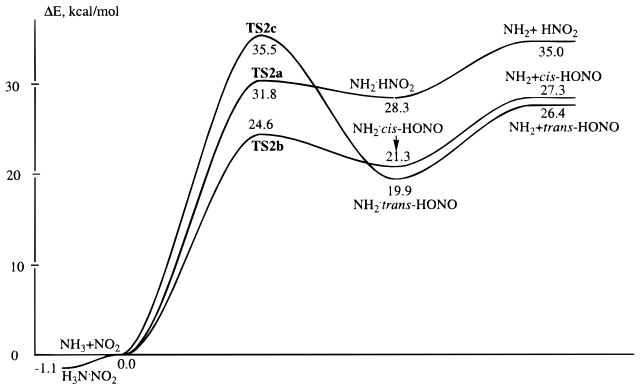

Figure 6. Profile of potential energy surface for the $NH_3 + NO_2$ reaction calculated at the G1(PU)//UMP2/6-311G(d,p) level.

reaction for (2a) and (2b) are higher by 0.9 and 8.6 kcal/mol, respectively, than that of (2c) with the G1(PU) approximation.

The ground electronic state of NH_2 is $^2B_1$, and the lowest excited state is $^2A_1$. At the UMP2/6-311G(d,p) level, the vertical and adiabatic excitation energies are high, 51.4 and 33.2 kcal/mol, respectively. Therefore, the $^2A_1$ state of NH_2 is not expected to be relevant to the reaction kinetics.

On the reactant side of the potential energy surface, we located a weak $H_3N{\cdot}NO_2$ complex with a binding energy of only 1.1 kcal/mol at the G1(PU) level. It has C_s symmetry, and the symmetry plane coincides with the bisector of ONO and one of the HNH angles. The complex is irrelevant to the hydrogen-abstraction reactions. Neither $H_2NH{\cdots}ONO$ nor $H_2NH{\cdots}NO_2$ complexes was found.

Reaction 2b is calculated to have the lowest barrier of the three, at the transition state TS2b, which lies by 39.6 kcal/mol higher than $NH_3 + NO_2$ at the UMP2 + ZPE level. The use of the G1(PU) method lowers the relative energy of TS2b by 15 kcal/mol. At this level of theory, TS2b is lower in energy by 2.7 kcal/mol than the NH_2 + *cis*-HONO products, and it cannot be directly connected to them. Tracing of the potential energy surface down from TS2b leads to the $NH_2{\cdot}$*cis*-HONO complex. The latter is 6 kcal/mol more stable than NH_2 + *cis*-HONO. No reverse barrier exists between the complex and the products. Both TS2b and $NH_2{\cdot}$*cis*-HONO have C_s symmetry. In TS2b, the N···H···ONO fragment is planar, and the remaining two hydrogens are reflected by this plane.

Reaction 2c has a much higher barrier at transition state TS2c, 48.0 and 35.5 kcal/mol at the UMP2 + ZPE and G1(PU) levels, respectively. The structure of the $NH_2{\cdot}$*trans*-HONO complex formed after TS2c is similar to that of $NH_2{\cdot}$*cis*-HONO. The *trans* complex is 1.4 kcal/mol more stable than the *cis* one, reflecting the energy difference between *trans*- and *cis*-HONO isomers. The complexation energy for $NH_2{\cdot}$*trans*-HONO is calculated to be 6.5 kcal/mol at the G1(PU) level, close to the corresponding value for $NH_2{\cdot}$*cis*-HONO. The $NH_2{\cdot}$*trans*-HONO complex dissociates to NH_2 and HONO without reverse barrier.

As seen in Table 4 and Figure 6, despite the fact that the two reactions, (2b) and (2c), are essentially the same except that (2b) is *cis* and (2c) is *trans*, (2b) has a low barrier while (2c) has a very high barrier at all levels of theory. The two potential energy profiles even cross, violating the so-called Hammond rule. While both reactions are endothermic, the transition states TS2b and TS2c at the UMP2 level seem to exhibit an early character; the breaking N···H bonds are stretched by only 0.07−0.14 Å as compared to that in NH_3 and the forming H···O bonds are still longer by 0.37−0.43 Å than the OH distance in HONO. These unexpected results require a careful theoretical consideration. The first possibility is that the large energy difference between the *cis* and *trans* TS's and an unusual character of their geometries are artifacts of the UMP2 geometry optimization. Therefore, we reoptimized the geometries of TS2b and TS2c using the hybrid density functional B3LYP method[25] with the same 6-311G(d,p) basis set. The B3LYP-optimized parameters are shown in italics in Figure 5. The geometry of the N···H···O fragment changes significantly. In TS2b, the N···H distance lengthens from 1.16 to 1.44 Å from UMP2 to B3LYP, and the H···O distance shortens from 1.35 to 1.10 Å. Similar, though less dramatic, changes are found for the N···H···O fragment in TS2c. Thus, the character of the transition states at the B3LYP level is much later than that at the UMP2 level, although the energies of reaction at the two levels are similar: about 33 kcal/mol for UMP2 and about 30 kcal/mol for B3LYP. Despite of the differences in the geometries, the QCISD(T)/6-311G(d,p) and G1(PU) energies of TS2b and TS2c are very similar for the UMP2- and B3LYP-optimized structures, as shown in Table 5. This means that the potential energy surface profile is flat in this area and the energy is not sensitive to the geometry of the N···H···O fragment. At all theory levels, the energy of TS2c is substantially (8−13 kcal/mol) higher than the energy of TS2b, supporting the conclusion made from the G1(PU)//UMP2 calculations.

The geometry of the other fragment, ONO, however, is more essential for the energetics at the transition states. In TS2b, the two NO bond lengths are virtually the same, while in TS2c, the ON bond adjacent to the forming OH bond is stretched by 0.15 Å, as compared to the bond in NO_2, indicating the breach of the ON π bond. The B3LYP method qualitatively reproduces the same trend, although it gives a somewhat larger alteration

TABLE 4: Total (hartrees) and Relative (kcal/mol) Energies of Various Structures through the $NH_3 + NO_2$ Reaction, Calculated at the UMP2/6-311G(d,p) and G1(PU) Levels of Theory

		energies		
species	ZPE[a]	UMP2/ 6-311G(d,p)	UMP2/ 6-311G(d,p) +ZPE	G1(PU)
$NH_3 + NO_2$[b]	27.1	−261.065 81	−261.022 62	−221.283 03
NH_2 + *trans*-HONO	23.7	36.8	33.4	26.4
NH_2 + *cis*-HONO	23.8	36.3	33.0	27.3
$NH_2 + HNO_2$	25.0	40.8	38.7	35.0
$NH_2{\cdot}$*trans*-HONO	25.8	26.6	25.3	19.9
$NH_2{\cdot}$*cis*-HONO	25.8	27.1	25.8	21.3
$NH_2{\cdot}HNO_2$	26.9	31.2	31.0	28.3
$H_3N{\cdot}NO_2$	28.9	−2.9	−1.2	−1.1
TS2a	25.0	43.4	41.3	31.8
TS2b	25.6	41.1	39.6	24.6
TS2c	24.4	50.7	48.0	35.5
R5[c]		37.1	34.7	
R4[c]		38.3	36.1	
R3[c]		39.8	38.2	
R2[c]	25.9	40.5	39.1	22.3
R1[c]	25.7	40.9	39.3	23.4
F1[c]	25.5	40.9	39.1	25.8
F2[c]	25.5	40.4	38.6	26.9
F3[c]	25.7	39.6	38.0	27.7
F4[c]	26.2	38.6	37.5	28.4
F5[c]	26.9	37.5	37.1	28.9
F6[c]		36.6		
F7[c]		35.3		

[a] Zero-point vibrational energies are calculated at the UMP2/6-311G(d,p) level and scaled by 0.95. [b] Total energies. Relative energies in the rest of the table are given with respect to $NH_3 + NO_2$. [c] The structures along IRC in the vicinity of TS2b. The reaction coordinate *s* value is −0.5 to −0.1 amu$^{1/2}$·bohr for R5−R1 and 0.1−0.7 for F1−F7.

TABLE 5: Energies (kcal/mol, ZPEs Are Included) of TS2b and TS2c Relative to $NH_3 + NO_2$ at Various Levels of Theory

	UMP2 geometry			B3LYP geometry		
	UMP2/6-311G(d,p)	QCISD(T)/6-311G(d,p)	G1(PU)	B3LYP/6-311G(d,p)	QCISD(T)/6-311G(d,p)	G1(PU)
TS2b	39.6	25.0	24.6	20.1	23.2	24.6
TS2c	48.0	33.7	35.5	28.2	33.5	37.5

of the ON bonds in TS2b. The energy for the $H_2N\cdots H\cdots ONO$ transition-state structures relative to $NH_3 + NO_2$ can be expressed as

$$E = E_{NH_3\text{-def}} + E_{NO_2\text{-def}} + E_{int} \quad (3a)$$

where $E_{NH_3\text{-def}}$ is the deformation energy of the NH_3 fragment in the $H_2N\cdots H\cdots ONO$ structure as compared to the free NH_3 molecule and $E_{NO_2\text{-def}}$ is the energy of NO_2 deformation. E_{int} is the interaction energy between the deformed fragments and is a function of geometries of both fragments and of their mutual location. The energy of TS2b, 41.1 kcal/mol at the UMP2 level, can be divided following eq 3a as

$$E(\text{TS2b; UMP2}) = 41.1 = 13.1 + 15.2 + 12.8 \quad (3b)$$

If one takes the optimized geometry of TS2b and changes the conformation from *cis* to *trans*, this "*trans*-TS2b" structure has

$$E(\textit{trans}\text{-TS2b; UMP2}) = 83.2 = 13.1 + 15.2 + 54.9 \quad (3b')$$

a large repulsion between the fragments. The trend is confirmed by the B3LYP calculations, which give the *trans*-TS2b structure 9 kcal/mol higher than the optimized TS2b. The higher repulsion energy for the *trans* conformation can be attributed to the repulsive interaction between an unpaired electron of NO_2 ($^2A_1$), located on the nitrogen p orbital directed outside of the ONO angle, and the forming O···H bond. This is supported by the data of populations analysis. In *trans*-TS2b, the spin density on the nitrogen atom of NO_2 is 0.56 e, close that in free NO_2, 0.52 e. Even though geometrically the ON π bond is not broken, the electronic structure of *trans*-TS2b corresponds to the broken bond; the spin density on the oxygen atom is 0.91 vs −0.02 in *cis*-TS2b.

In TS2c, the ON π bond is broken, the unpaired electron is shifted to the oxygen atom, and it participates in the formation of the O···H bond. The calculated spin density on N of NO_2 decreases to −0.14 e, while the spin density on the oxygen, participating in the bond formation, is 0.88. The energy of TS2c can be decomposed as

$$E(\text{TS2c; UMP2}) = 50.7 = 2.1 + 34.3 + 14.3 \quad (3c)$$

Comparison of eq 3c and 3b′ suggests that the reason for the high barrier is the repulsive interaction between NO_2 and NH_3; the repulsion energy is so high for *trans*-TS2b that the system chooses to break the ON π bond to find the lower TS2c, which is still substantially higher in energy than TS2b. We have not found any *trans*-TS without breaking the ON π bond either at the UMP2 or the B3LYP level; optimization starting from *trans*-TS2b at both levels converges to TS2c. The geometry, where $E(H_2N\cdots H\cdots ONO)$ reaches a saddle point, is determined by the behavior of $E_{NH_3\text{-def}}$, $E_{NO_2\text{-def}}$, and E_{int}, contributing to the overall energy. E_{int} behaves differently for *cis* and *trans* conformations. In order to illustrate this, we calculated E_{int} for *cis* and *trans* conformations at different HO distances maintaining geometries of the NH_3 and NO_2 fragments unchanged, as in free molecules. Figure 7 shows E_{int} for the *cis* and *trans* cases, calculated at the B3LYP level, and the spin density on the nitrogen atom of NO_2. One can see that $E_{int}(\textit{trans})$ is higher than $E_{int}(\textit{cis})$ for H−O ≥ 1.2 Å. The highest difference, 10−12 kcal/mol, is found for H−O in the 1.3−1.5-Å range. At H−O = 1.1 Å, the electronic structure of the system changes even though the fragment geometries are not allowed to change. Spin density is shifted from the N atom to the O atom in NO_2, and $E_{int}(\textit{cis})$ becomes somewhat higher than $E_{int}(\textit{trans})$.

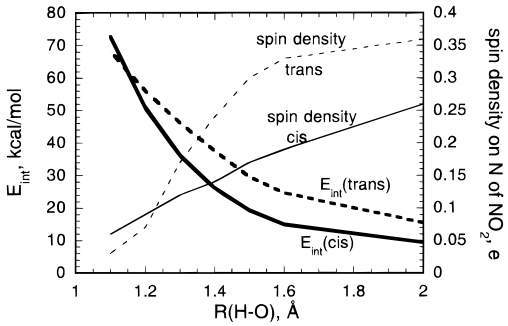

Figure 7. Interaction energy between the nondeformed NH_3 and NO_2 fragments and spin density on the nitrogen atom of NO_2 in *cis* and *trans* conformations as functions of the H−O distance.

Reaction 2a produces the HNO_2 isomer which is 8.6 kcal/mol less stable than *trans*-HONO. The hydrogen is abstracted during the course of the reaction from nitrogen by the attacking nitrogen atom. Therefore, the structure of transition state TS2a differs from those of TS2b and TS2c. It also rather resembles transition state TS1 for the $NH_3 + NO \rightarrow NH_2 + HNO$ reaction. The presence of the extra oxygen makes TS2a symmetric; N···H···N is the mirror plane, and two H and two O atoms are reflected by it. Though TS2a is a late TS, it is earlier than TS1. The breaking N···H bond is shorter, 1.308 Å in TS2a vs 1.534 Å in TS1, while the forming H···N bond is longer, 1.200 Å in TS2a vs 1.123 Å in TS1. This is attributed to the lower endothermicity of reaction 2a is compared to that of (1). The barrier for reaction 2a is 41.3 and 31.8 kcal/mol at the UMP2/6-311G(d,p) + ZPE and G1(PU) levels, respectively. On the product side, TS2a is connected to the $NH_2\cdot HNO_2$ complex, which is 6.7 kcal/mol more stable at the G1(PU) level than $NH_2 + HNO_2$, and its geometry is similar to those for the $NH_2\cdot$HONO complexes. $NH_2\cdot HNO_2$ is planar and possesses C_{2v} symmetry. Reaction 2a has significantly higher endothermicity than (2b) and is expected to be much slower than the latter.

Reaction Coordinate Tracing and VTST Calculations of the Rate Constant. Consideration of the potential energy surface for the $NH_3 + NO_2$ reaction shows that it is dominated by channel 2b, giving NH_2 and *cis*-HONO. Therefore, in this section, we first calculate the rate constant for this channel. The transition state TS2b is lower in energy than the product NH_2 + HONO. However, at 300 K, the relative ΔG^* of TS2b is 34.9 kcal/mol, while that of NH_2 + *cis*-HONO is 26.6 kcal/mol, with the energies and frequencies calculated at the G1-(PU) and UMP2/6-311G(d,p) levels, respectively. At higher temperatures, the entropy contribution to ΔG^* becomes increasingly significant, and the tight TS2b structure has a higher free energy than NH_2 + HONO. Since we are interested in the rate constant at combustion temperatures, we consider the $NH_3 + NO_2 \rightarrow$ TS2b $\rightarrow NH_2$−*cis*-HONO step as rate-controlling. In order to calculate the rate based on the VTST theory, we performed IR calculations in the vicinity of TS2b, for the reaction coordinate *s* value between −0.5 and +0.8 amu$^{1/2}$·bohr.

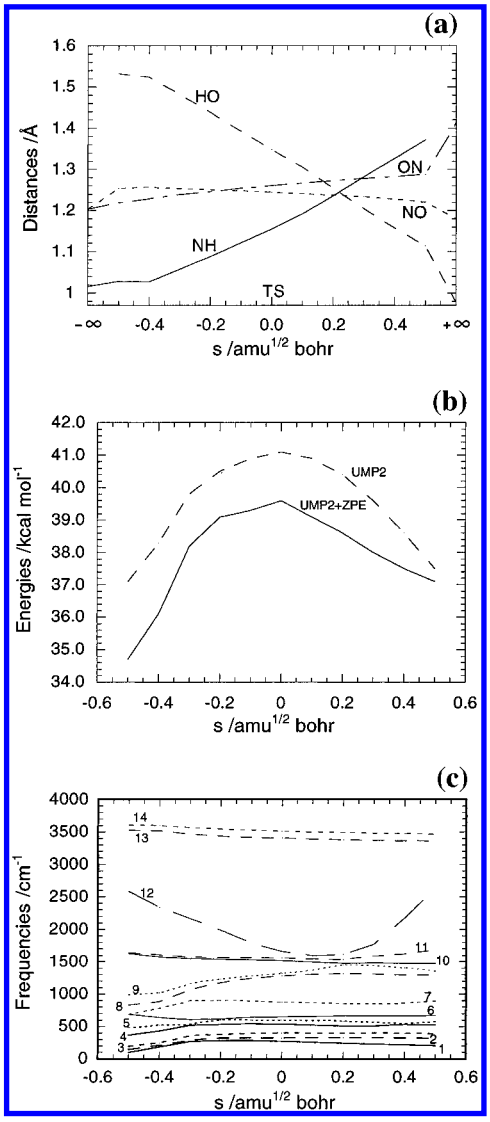

Figure 8. (a) Changes of some geometric parameters for the $NH_3 + NO_2$ system along IRC for channel 2b as a function of the reaction coordinate *s*. (b) Changes of the relative UMP2/6-311G(d,p) and UMP2/6-311G(d,p) + ZPE energies along IRC as functions of *s*. (c) Changes of vibrational frequencies for the $NH_3 + NO_2$ system as functions of *s*.

The changes of the bond distances along IRC are shown in Figure 8a. One can see the increase of the NH distance for the breaking bond and the decrease of the HO distance for the forming bond. The ON bond turns from a double one into a single bond, while the second NO bond length changes only slightly. In the interval of $-0.5 \le s \le 0.8$ amu$^{1/2}$·bohr, the ONO angle decreases from 118.0 to 115.7°. Therefore, the major change of this angle, from 134 to 118°, occurs before $s = 0.5$. The closure of the ONO angle in NO_2 while it apparoaches NH_3 leads to the energy loss of 37.1 kcal/mol (UMP2/6-311G(d,p)) from $s = -\infty$ to -0.5. In the NO_2 fragment, the corresponding energy change due to geometry distortion is 11.8 kcal/mol, the deformation of NH_3 costs only 4.3 kcal/mol, and the repulsion of the fragments at this phase is, therefore, 21.0 kcal/mol.

The frequency change along IRC is shown in Figure 8c. One can see that the frequency Q_{12} changes significantly during the reaction. It corresponds to the NH stretch in the NH_3 reactant (3349 cm^{-1}) and to the OH stretch in HONO (3473 cm^{-1}). While the NH bond is breaking and OH is forming, the Q_{12} frequency decreases, reaches a minimum at $s = +0.2$ amu$^{1/2}$·bohr (1600 cm^{-1}), and then rises.

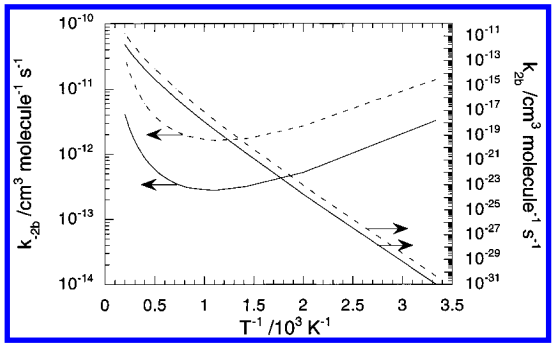

Figure 9. Arrhenius plot of the forward and reverse rate constants for the $NH_3 + NO_2 \rightarrow NH_2 + cis$-HONO reaction. Solid and dashed curves show the rate constants calculated with UMP2 and B3LYP molecular parameters, respectively.

As for the $NH_3 + NO$ reaction, we performed VTST calculations for the rate-controlling reaction (2b), $NH_3 + NO_2 \rightarrow$ TS2b $\rightarrow NH_3$·*cis*-HONO. For ΔG^* computations, we used vibrational frequencies of the reactants and the structures along IRC (R5−R1, TS2b, F1−F5), shown in Table 6, and their moments of inertia from Table 7. For maximization of ΔG^* at various temperatures, UMP2/6-311G(d,p) + ZPE energies fitted to a polynomial were used. Once the maxima were located, the energy contribution in ΔG^* was corrected using G1(PU) energies of the IRC structures.

The transition-state locations were found between TS2b and R1 in the interval of $-0.07 \le s \le -0.01$ amu$^{1/2}$·bohr. The three-parameter expression for the calculated rate constant k_{2b} fitted in the temperature range of 300−5000 K is given by

$$k_{2b} = 1.22 \times 10^{-23} T^{3.30} \exp(-11\,217/T)\ \text{cm}^3/(\text{molecule·s})$$

The Arrhenius plots for k_{2b} and the reverse rate constant computed by $k_{-2b} = k_{2b}/K_{2b}$ are shown in Figure 9. k_{-2b} exhibits a significant negative temperature dependence at $T \le 1000$ K, reflecting the formation of the NH_2·*cis*-HONO complex at low temperatures, as mentioned before. The following three-parameter expression for k_{-2b} was obtained by fitting the calculated values covering the temperature range of 300−5000 K:

$$k_{-2b} = 3.49 \times 10^{-23} T^{2.93} \exp(2579/T)\ \text{cm}^3/(\text{molecule·s})$$

The use of B3LYP-optimized geometries for the reactants, products, and TS2b does not change the reaction energetics. If one employs the B3LYP frequencies and moments of inertia for the rate constant calculations with a conventional TST approach, the fitted three-parameter expressions for k_{2b} and k_{-2b} are the following:

$$k_{2b} = 3.92 \times 10^{-23} T^{3.41} \exp(-11\,301/T)\ \text{cm}^3/(\text{molecule·s})$$

$$k_{-2b} = 1.18 \times 10^{-22} T^{3.02} \exp(2487/T)\ \text{cm}^3/(\text{molecule·s})$$

The rate constant values increase by 3−4 times, because the transition-state structure is looser at the B3LYP level as compared to that at UMP2.

The calculated equilibrium constants,

$$K_{2b} = 7.29 \exp(-14\,131/T)$$

(UMP2 molecular parameters)

$$K_{2b} = 7.54 \exp(-14\,133/T)$$

(B3LYP molecular parameters)

agree fairly well with the JANAF equilibrium constant,

$$K_{2b} = 8.87 \exp(-15\,524/T)$$

For reactions 2a and 2c, the hydrogen-abstraction steps leading to the formation of the NH_2·HNO_2 and NH_2·*trans*-

TABLE 6: Scaled UMP2/6-311G(d,p) Normal Vibrational Frequencies (cm^{-1}) for Intermediates, Transition States, and the Structures along the IRC of the Reaction of NH_3 and NO_2

species	ω_1	ω_2	ω_3	ω_4	ω_5	ω_6	ω_7	ω_8	ω_9	ω_{10}	ω_{11}	ω_{12}	ω_{13}	ω_{14}	ω_{15}
$NH_3 + NO_2$							736[a]	1073[b]	1319[a]	1593[b]	1593[b]	2326[c]	3349[b]	3485[b]	3485[b]
NH_2 + *trans*-HONO							559[d]	606[d]	820[d]	1243[d]	1467[e]	1602[d]	3275[e]	3369[e]	3649[d]
NH_2 + *cis*-HONO							632[f]	686[f]	899[f]	1272[f]	1467[e]	1556[f]	3275[e]	3369[e]	3473[f]
$NH_2 + HNO_2$							754[g]	1004[g]	1303[g]	1467[e]	1479[g]	1743[g]	3117[g]	3275[e]	3369[e]
NH_2·*trans*-HONO	13	72	125	208	293	325	687	885	919	1395	1468	1589	3312	3361	3413
NH_2·*cis*-HONO	74	82	148	200	296	326	679	931	992	1369	1461	1544	3207	3309	3413
NH_2·HNO_2	32	52	177	183	285	377	748	1131	1300	1469	1568	1714	3042	3310	3410
H_3N·NO_2	44	49	57	109	133	148	737	1078	1325	1586	1591	3071	3374	3483	3483
TS2a	2634*i*	72	146	251	481	653	765	819	1194	1343	1485	1512	1696	3288	3383
TS2c	2182*i*	132	160	177	307	578	662	777	894	1478	1519	1693	1848	3376	3471
TS2c[h]	*1513i*	*114*	*148*	*169*	*411*	*583*	*663*	*790*	*890*	*1357*	*1545*	*1603*	*1680*	*3438*	*3531*
R5[i]		96	143	191	361	480	687	690	832	993	1628	1641	2580	3526	3604
R4[i]		181	202	244	430	522	638	783	883	1016	1574	1606	2337	3519	3601
R3[i]		264	286	352	517	530	607	899	1069	1157	1546	1574	2162	3467	3568
R2[i]		283	323	371	532	600	617	903	1172	1231	1536	1564	1984	3438	3544
R1[i]		281	319	391	542	599	645	893	1239	1281	1527	1560	1789	3417	3525
TS2b	1114*i*	269	323	396	536	597	651	880	1281	1321	1514	1558	1659	3403	3512
TS2b[h]	*470i*	*192*	*194*	*261*	*493*	*604*	*745*	*971*	*1319*	*1320*	*1520*	*1566*	*1729*	*3426*	*3520*
F1[i]		255	326	395	520	592	656	865	1308	1370	1497	1547	1600	3391	3501
F2[i]		238	325	394	505	581	661	855	1318	1450	1473	1533	1614	3379	3490
F3[i]		224	324	396	507	565	666	852	1312	1442	1479	1586	1772	3371	3481
F4[i]		213	319	394	530	543	666	861	1299	1405	1477	1625	2176	3365	3474
F5[i]		199	314	399	50	574	667	895	1297	1357	1475	1678	2632	3359	3468

[a] NO_2 frequency. [b] NH_3 frequency. [c] This frequency of NO_2 is overestimated at the UMP2/6-311G(d,p) level. The corresponding values at the QCISD/6-311G(d,p) level and in experinment are 1663 and 1666^{-1}, respectively. [d] *trans*-HONO frequency. [e] NH_2 frequency. [f] *cis*-HONO frequency. [g] HNO_2 frequency. [h] Italic numbers show unscaled B3LYP/6-311G(d,p) frequencies. [i] For the structures along IRC $3N - 7$ frequencies, projected out of the reaction coordinate, were calculated.

TABLE 7: Moments of Inertia (10^{-40} g × cm^2) for the Various Structures through the $NH_3 + NO_2$ Reaction, Optimized at the UMP2/6-311G(d,p) Level

species	I_x	I_y	I_z
NH_3	2.850	2.850	4.420
NO_2	3.606	65.603	69.210
NH_2	1.228	2.140	3.368
trans-HONO	9.047	66.860	75.907
cis-HONO	10.090	63.240	73.330
HNO_2	7.911	65.030	72.941
NH_2·*trans*-HONO	24.884	308.618	333.502
NH_2·*cis*-HONO	61.819	207.748	269.568
NH_2·HNO_2	70.268	239.320	306.309
H_3N·NO_2	72.780	195.216	257.833
TS2a	68.288	168.652	234.221
TS2b	63.338	118.720	177.406
TS2b[a]	*65.113*	*138.255*	*198.889*
TS2c	24.076	232.841	253.114
TS2c[a]	*23.590*	*245.877*	*266.588*
R5	62.293	118.988	176.591
R4	62.605	119.103	177.029
R3	62.834	119.024	177.169
R2	63.029	118.924	177.270
R1	63.193	118.782	177.307
F1	63.452	118.675	177.496
F2	63.580	118.728	177.701
F3	63.672	118.748	177.837
F4	63.748	118.815	178.007
F5	63.815	118.981	178.270

[a] Italic numbers show the moments of inertia for the B3LYP/6-311G(d,p)-optimized geometries.

HONO complexes are also important at temperatures > 300 K. Assuming that variation along IRC does not affect the rate much, as is the case for 2b, we calculated CTST rate constants for these channels using molecular parameters of TS2a and TS2c. The fitted rate coefficients in are as follows:

$$k_{2a} = 4.07 \times 10^{-24} T^{3.41} \exp(-15\,036/T)\ \mathrm{cm^3/(molecule{\cdot}s)}$$

$$k_{2c} = 8.15 \times 10^{-24} T^{3.69} \exp(-16\,610/T)\ \mathrm{cm^3/(molecule{\cdot}s)}$$

At 300 K, reaction 2b is by 5 and 8 orders of magnitude faster than (2a) and (2c), respectively. At 1000 K, the rate constant for (2b) is about 6 and 21 times higher than those for (2a) and (2c). At very high temperatures, such as 5000 K, all three rate coefficients are of the same order of magnitude. The total rate constant for reaction 2, $k_2 = k_{2a} + k_{2b} + k_{2c}$, calculated at the G1 level of theory, is expressed as

$$k_2 = 2.87 \times 10^{-29} T^{5.10} \exp(-10\,389/T)\ \mathrm{cm^3/(molecule{\cdot}s)}$$

In the above calculations, we did not consider tunneling corrections for the rate constants. For reactions 2a and 2b, the energies of the transition states with zero-point corrections are below the product asymptotes, and the barriers above the products exist only on the Gibbs free-energy surfaces, at temperatures higher than 300 K. Therefore, tunneling can be neglected for (2a) and (2b). Reaction 2c has a barrier above the product asymptote, and we calculated the tunneling correction given by[26] $Q_{\mathrm{tunnel}} = 1 - 1/24(h\nu_s/k_BT)^2(1 + k_BT/E_0)$, where ν_s is the TS2c imaginary frequency and E_0 is the barrier height with ZPE. The calculations show that at low temperatures, the correction is significant; at 300 and 500 K, the k_{2c} values with tunneling correction are 5.6 and 2.7 times higher than those without the correction, respectively. At higher temperatures, the effect of the tunneling correction decreases and becomes negligible. The three-parameter expression for k_{2c} with tunneling can be given by

$$k_{2c}(\mathrm{tunnel}) = 3.12 \times 10^{-23} T^{3.52} \exp(-16\,404/T)\ \mathrm{cm^3/(molecule{\cdot}s)}$$

The correction for k_{2c}, however, does not affect the total rate constant k_2, because tunneling is essential only at low temperatures where k_{2c} is many orders of magnitude smaller than k_{2b}, as mentioned above.

Concluding Remarks

The reactions of NH_3 with NO_x ($x = 1, 2$) proceed by abstraction of hydrogen atom from ammonia to produce NH_2

and HNO ($x = 1$) and HONO or HNO_2 ($x = 2$). Both reactions are calculated to be endothermic, and the calculated heats of reaction are in good agreement with experimental measurements. Reaction 1, $NH_3 + NO \rightarrow NH_2 + HNO$, was found to have a transition state at the UMP2/6-311G(d,p) level; however, it disappeared at the higher G2(PU) level. The rate constants for (1) and the reverse $NH_2 + HNO \rightarrow NH_3 + NO$ reaction were computed by VTST in conjunction with detailed balancing. k_{-1} was found to be smaller than that of the isoelectronic $OH + HNO \rightarrow H_2O + NO$ reaction, reflecting the lower reactivity of NH_2 and the exothermicity of the $NH_2 + HNO$ reaction, although neither has a barrier.

The reaction of NH_3 with NO_2 can occur by three channels, leading to HNO_2, *cis*-HONO, and *trans*-HONO. All three mechanisms involve two steps: (1) abstraction of hydrogen from NH_3 with the formation of $NH_2 \cdot HNO_2$ or $NH_2 \cdot HONO$ complexes; (2) dissociation of the complexes. The first step has the barriers of 31.8, 24.6, and 35.5 kcal/mol at the G1(PU) level for channels 2a, 2b, and 2c, respectively. Thus, mechanism 2b producing *cis*-HONO is expected to be dominant in the reaction. The complexes of NH_2 with various isomers of HNO_2 species are stabilized by 6−7 kcal/mol with respect to the products and dissociate without barrier. For (2a) and (2b) channels, the abstraction transition states lie below the products in energy, and the second step is rate-controlling at low temperatures. However, at ambient temperature and higher, the entropy contribution makes the first hydrogen-abstraction step rate-determining; the Gibbs free energies of TS2a and TS2b are much higher than that of the products. Therefore, the VTST rate constants for reactions 2a and 2b were calculated by using molecular parameters of the transition states for the first reaction step. An experimental study of the rate constant for reaction 2 is underway. The theoretical activation energy, $E_a = 25.6$ kcal/mol, evaluated with data below 1000 K, where most reliable experiments for the abstraction process have been carried out, agrees closely with the averaged experimental value, $E_a = 27 \pm 2$ kcal/mol.[14,27,28]

Acknowledgment. We gratefully acknowledge the support of this work by the Office of Naval Research (Contract No. N00014-89-J-1949) and to the Cherry L. Emerson Center for Scientific Computation for the use of various programs and computing facilities.

References and Notes

(1) Miller, J. A.; Bowman, C. T. *Prog. Energy Comust. Sci.* **1989**, *15*, 287.

(2) Glarborg, P.; Dam-Johansen, K.; Miller, J. A.; Kee, R. J.; Coltrin, M. E. *Int. J. Chem. Kinet.* **1994**, *26*, 421.

(3) Hanson, R. K.; Salimian, S. In *Combustion Chemistry*; Gardiner, W. C., Ed.; Springer-Verlag: New York, 1984; p 361.

(4) Brill, T. B.; Brush, P. J.; Patil, D. G. *Combust. Flame* **1993**, *92*, 7788.

(5) Mebel, A. M.; Lin, M. C.; Morokuma, K.; Melius, C. F. *J. Phys. Chem.* **1995**, *99*, 6842.

(6) Lin, M. C.; He, Y.; Melius, C. F. *Int. J. Chem. Kinet.* **1992**, *24*, 489.

(7) Diau, E. W. G.; Yu, T.; Wagner, M. A. G.; Lin, M. C. *J. Phys. Chem.* **1994**, *98*, 4034.

(8) Diau, E. W. G.; Lin, M. C.; He, Y.; Melius, C. F. *Progress. Energ. Combust. Sci.* **1995**, *21*, 1.

(9) Mebel, A. M.; Morokuma, K.; Lin, M. C. *J. Chem. Phys.* **1994**, *101*, 3916.

(10) Diau, E. W. G.; Halbgewachs, M.; Lin, M. C. *Int. J. Chem. Kinet.* **1995**, *27*, 867.

(11) Diau, E. W. G.; Lin, M. C. *J. Phys. Chem.* **1995**, *99*, 6589.

(12) Mebel, A. M.; Hsu, C.-C.; Morokuma, K.; Lin, M. C. *J. Chem. Phys.*, **1995**, *103*, 5640.

(13) Park, J.; Lin, M. C. *J. Phys. Chem.* **1996**, *100*, 3317.

(14) Thaxton, A. G.; Lin, M. C. In preparation.

(15) (a) Garrett, B. C.; Truhlar, D. G. *J. Chem. Phys.* **1979**, *70*, 1593. (b) Isaacson, A. D.; Truhlar, D. G. *J. Chem. Phys.* **1982**, *76*, 1380.

(16) Hehre, W.; Radom, L.; Schleyer, P. v. R.; Pople, J. A. *Ab Initio Molecular Orbital Theory*; Wiley: New York, 1986.

(17) (a) Pople, J. A.; Head-Gordon, M.; Fox, D. J.; Raghavachari, K.; Curtiss, L. A. *J. Chem. Phys.* **1989**, *90*, 5622. (b) Curtiss, L. A.; Jones, C.; Trucks, G. W.; Raghavachari, K.; Pople, J. A. *J. Chem. Phys.* **1990**, *93*, 2537. (c) Curtiss, L. A.; Raghavachari, K.; Trucks, G. W.; Pople, J. A. *J. Chem. Phys.* **1991**, *94*, 7221.

(18) Mebel, A. M.; Morokuma, K.; Lin, M. C.; Melius, C. F. *J. Phys. Chem.* **1995**, *99*, 1900.

(19) Frisch, M. J.; Trucks, G. W.; Head-Gordon, M.; Gill, P. M. W.; Wong, M. W.; Foresman, J. B.; Johnson, B. G.; Schlegel, H. B.; Robb, M. A.; Replogle, E. S.; Gomperts, R.; Andres, J. L.; Raghavachari, K.; Binkley, J. S.; Gonzales, C.; Martin, R. L.; Fox, D. J.; DeFrees, D. J.; Baker, J.; Stewart, J. J. P.; Pople, J. A. *GAUSSIAN 92/DFT*; Gaussian, Inc.: Pittsburgh, PA, 1993.

(20) Gonzalez, C.; Schlegel, B. H. *J. Chem. Phys.* **1989**, *90*, 2154.

(21) Soto, M. R.; Page, M.; McKee, M. L. *Chem. Phys.* **1991**, *153*, 415.

(22) Jensen, F. *Chem. Phys. Lett.* **1990**, *169*, 519.

(23) Roose, T. R.; Hanson, R. K.; Kruger, C. H. *Shock Tube Shock Wave Res. Proc. Int. Symp.* **1977**, *11*, 245.

(24) Chase, M. W., Jr.; Davies, C. A.; Downey, J. R., Jr.; Frurip, D. J.; Mcdonald, R. A.; Syverud, A. N. JANAF Thermochemical Tables. *J. Phys. Chem. Ref. Data* **1985**, *14*, Suppl. 1.

(25) (a) Becke, A. D. *J. Chem. Phys.* **1993**, *98*, 5648. (b) Lee, C.; Yang, W.; Parr, R. G. *Phys. Rev. B* **1988**, *37*, 785.

(26) Steinfield, J. I.; Francisco, J. S.; Hase, W. L. *Chemical Kinetics and Dynamics*; Prentice-Hall: Englewood Cliffs, NJ, 1989.

(27) Rosser, W. A.; Wise, H. *J. Chem. Phys.* **1956**, *25*, 1078.

(28) Bedford, G.; Thomas, J. H. *J. Chem. Soc., Faraday Trans.* **1972**, *1*, 68.

JP953644F